

## Coupled pair of one- and two-dimensional magnetoplasmons on electrons on helium

A. D. Chepelianskii,<sup>1</sup> D. Papoular,<sup>2</sup> D. Konstantinov,<sup>3</sup> H. Bouchiat,<sup>1</sup> and K. Kono<sup>4</sup>

<sup>1</sup>*LPS, Université Paris-Saclay, CNRS, UMR 8502, F-91405, Orsay, France*

<sup>2</sup>*Laboratoire de Physique Théorique et Modélisation, CNRS UMR 8089, CY Cergy Paris Université, 95302 Cergy-Pontoise Cedex, France*

<sup>3</sup>*Okinawa Institute of Science and Technology (OIST) Graduate University, Onna, Okinawa 904-0412, Japan*

<sup>4</sup>*ICST, NCTU, 1001 Ta Hsueh Road, Hsinchu 300, Taiwan*



(Received 21 October 2019; revised 13 January 2021; accepted 13 January 2021; published 12 February 2021)

Electrons on the liquid helium surface form an extremely clean two-dimensional system where different plasmon excitations can coexist. Under a magnetic field, time-reversal symmetry is broken, and all the bulk magnetoplasmons become gapped at frequencies below cyclotron resonance while chiral one-dimensional edge magnetoplasmons appear at the system perimeter. We theoretically show that the presence of a homogeneous density gradient in the electron gas leads to the formation of a delocalized magnetoplasmon mode in the same frequency range as the lowest-frequency edge-magnetoplasmon mode. We experimentally confirm its existence by measuring the corresponding resonance peak in frequency dependence of the admittance of the electron gas. This allows us to realize a prototype system to investigate the coupling between a chiral one-dimensional mode and a single delocalized bulk mode. Such a model system can be important for the understanding of transport properties of topological materials where states of different dimensionality can coexist.

DOI: [10.1103/PhysRevB.103.075420](https://doi.org/10.1103/PhysRevB.103.075420)

### I. INTRODUCTION

The recent discovery of topological states of matter has led to striking predictions of topological surfaces and edge states [1–11]. However, it has so far been difficult to realize a system where topological edge states are completely decoupled from remaining bulk states or spurious edge states of nontopological origin [10–13]. Thus understanding the interaction between topological edge modes and nontopological bulk modes is highly important. Electrons on helium are a high-purity two-dimensional system where chiral edge-magnetoplasmon modes naturally form under a perpendicular magnetic field [14–17]; interestingly, their topological origin has been recognized only recently [18–20]. Bulk magnetoplasmons in a two-dimensional electron gas have a gap at frequencies below the cyclotron resonance, and it is traditionally considered that edge and acoustic magnetoplasmons are the only low-frequency plasmon excitations [21–23]. In experiments with electrons on helium the frequency of edge magnetoplasmons (EMPs) is typically in the kilohertz range, while the cyclotron resonance frequency is typically several gigahertz. We show how a low-energy bulk mode can be created inside the bulk-magnetoplasmon gap by an anisotropic gradient of electronic density. In this paper we will describe this plasma excitation as a magnetogradient mode. We show that the frequency of this magnetogradient mode can be obtained from an effective Schrödinger equation allowing us to control the resonance frequency through the shape of the electron cloud. This allows us to tune this frequency into resonance with the edge magnetoplasmons creating a model setting to study the interaction between bulk and topological edge modes. We note that the existence of this low-frequency bulk magnetoplasmon can also be important to understand the surprising collective effects that appear in electrons on helium in the microwave-

induced resistance oscillation regime [24–30]: zero-resistance states [31,32], incompressibility [33,34], and self-oscillations [35], which are not yet understood microscopically.

### II. THEORETICAL DESCRIPTION OF THE GRADIENT MAGNETO-PLASMON

We first show that the presence of a density gradient can indeed lead to the formation of a low-frequency delocalized magnetoplasmon; this may seem counterintuitive as in a homogeneous system all the bulk magnetoplasmons are gapped with their lowest frequency given by the cyclotron frequency  $\omega_c = eB/m$ . The equations of motion for magnetoplasmons can be derived from the drift transport equations on the electronic density  $n_e = n_a + n_t$ , where we decompose the electronic density into time-averaged ( $n_a$ ) and time-dependent ( $n_t$ ) parts (see a sketch of the cell geometry in Fig. 1). Treating the time-dependent terms as a small perturbation, the linearized transport equations are

$$\partial_t n_t = \text{div}_{2d} [n_a (\mu_{xx} \nabla_{2d} V_t + \mu_{xy} \mathbf{u}_z \times \nabla_{2d} V_t)]. \quad (1)$$

Here,  $V_t$  is the time-dependent part of the quasistatic electric potential  $V = V_s + V_t$ , and  $V_s$  is its static part. In deriving this equation we took into account that the electron cloud screens the static part of the electronic potential, which leads to  $\nabla V_s = 0$ , and the longitudinal and Hall mobilities are given by  $\mu_{xx}$  and  $\mu_{xy}$ . Experiments typically take place in the high-magnetic-field regime  $\mu_{xx} \ll \mu_{xy}$  and  $\mu_{xy} \simeq B^{-1}$  (this corresponds to  $\omega_c$  much faster than the scattering rate). Hence it is reasonable to first find the frequency of the resonant plasmon modes in the limit  $\mu_{xx} = 0$ . The potential  $V_t$  can be determined from the time-dependent density  $n_t$  by solving the electrostatic Poisson equation; for simplicity we will

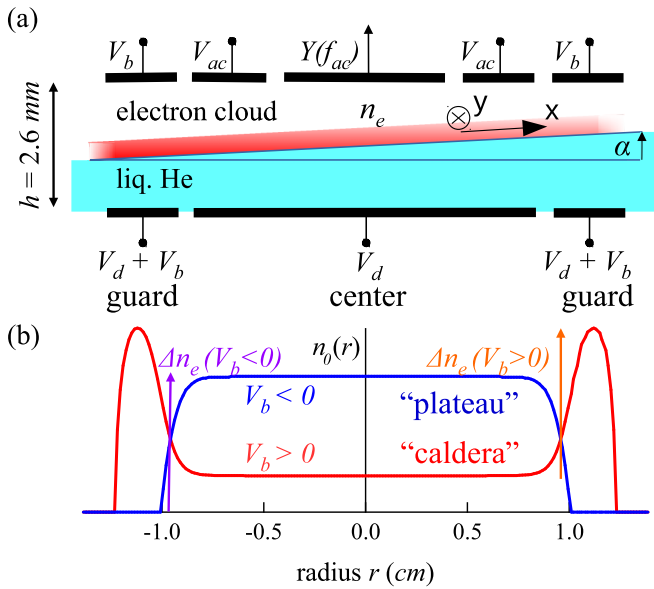


FIG. 1. (a) Sketch of the experimental cell with applied dc and ac voltages. The helium cell and electrodes have cylindrical symmetry, but the helium level is slightly tilted with an angle  $\alpha$ . A trapping potential  $V_d = 7$  V is applied to all bottom electrodes, and a bias voltage  $V_b$  can adjust the density between the outer guard and central regions. The cell admittance  $Y(f_{ac})$  at frequency  $f_{ac} = \omega/(2\pi)$  is measured between the top central and middle electrodes on which an ac potential  $V_{ac}$  at frequency  $f_{ac}$  is applied. (b) The typical “plateau” and “caldera” profiles, which occur at  $V_b < 0$ , respectively. Orange and purple arrows illustrate the two possible definitions of  $\Delta n_e$  in Eq. (4) for the two types of density profile. Liq., liquid.

assume for now a local electrostatics approximation  $n_t = \chi V_t$ , where the compressibility  $\chi = \frac{4\epsilon_0}{he}$  is obtained from a plane capacitor model. Simulations with an exact solution of electrostatic equations will be presented later. The static electron density in the presence of a density gradient can be written as  $n_a(r, \theta) = n_0(r) + n_{0c}(r) \cos \theta$ , where  $(r, \theta)$  are polar coordinates on the helium surface oriented along the gradient direction. Away from the edges of the electron gas, we can approximate  $n_{0c}(r) = \lambda r$  and treat the gradient  $\lambda$  as a small anisotropy parameter. It is thus natural to expand  $n_t$  and  $V_t$  in harmonics of the angle  $\theta$ :

$$n_t = n_{r0}(r) + n_{rc}(r) \cos \theta + n_{rs}(r) \sin \theta, \quad (2)$$

where we have kept the lowest harmonics. This procedure is justified since the only anisotropy comes from the uniform density gradient which couples only nearby harmonics through the  $\cos \theta$  term. Expanding to the lowest polar angle harmonics, we cast Eq. (1) into an effective Schrödinger equation which describes standing modes of electron-density oscillations:

$$\frac{\chi^2 \omega^2}{\mu_{xy}^2} \psi = -\frac{\lambda^2}{2} \partial_r^2 \psi + \frac{3\lambda^2}{8r^2} \psi + \frac{(\partial_r n_0)^2}{r^2} \psi. \quad (3)$$

In this equation we introduced the effective wave function  $\psi(r) = \sqrt{r} n_s$ , and  $\omega$  is the frequency of the density oscillation; its time dependence obeys  $\partial_t^2 \psi = -\omega^2 \psi$ . This equation describes a radial wave which propagates at velocity  $v =$

$\mu_{xy} \lambda / \sqrt{2} \chi$ . As in quantum mechanics, the shape of the wave function  $\psi$  is controlled by the external potential. From Eq. (3) we see that it contains a term describing repulsion at the origin and a confinement term proportional to the square of the gradient of the static isotropic density distribution  $(\partial_r n_0)^2$ . The obtained plasmon mode exists only due to the simultaneous presence of a magnetic field and of the anisotropic density gradient  $\lambda$ ; we will thus call it a gradient magnetoplasmon (GMP). The frequency,  $\omega_g$ , of the first GMP mode is given by the ground state of the Schrödinger equation (3); it scales as  $\omega_g \sim \mu_{xy} \lambda / (\chi R)$ , where  $R$  is the radius of the electron cloud. This frequency vanishes at the limit  $R \rightarrow \infty$ ; its behavior is thus similar to EMPs, which also do not have a gap and can have frequencies much below  $\omega_c$ . The GMP frequency drops to zero at  $\lambda = 0$  and will be overdamped if the density gradients are not strong enough. Fortunately, due to the high mobility of electrons on the helium system this mode can be visible even for small density gradients. Since Eq. (3) is a standing-wave equation, in addition to the lowest-frequency mode at frequency  $\omega_g$ , resonances are expected at its harmonics  $\omega_n = n\omega_g$  ( $n \geq 1$ , an integer); these harmonics will, however, turn out to be overdamped in our experiments.

The previous calculation showed that a small density gradient can create delocalized bulk-magnetoplasmon modes well below the cyclotron resonance frequency, which is usually believed to give the gap frequency for bulk magnetoplasmons. This calculation was performed using a local-density approximation  $n_t = \chi V_t$  and does not provide a complete description of the low-frequency magnetoplasmon modes. Indeed, Eq. (3) does not predict any finite frequency modes in the limit  $\lambda \rightarrow 0$ , and the edge-magnetoplasmon modes are thus missing. Hence a more realistic theory reproducing the already known magnetoplasmons is needed. Such a theory has to go beyond the local-density approximation and treat the long-range Coulomb interactions in a realistic way. This requires us to fix the electrostatic environment of the electron gas and its properties. From here we will focus on a realistic model of our experimental setup with electrons on helium.

### III. EXPERIMENTAL OBSERVATIONS

A sketch of the system is shown in Fig. 1: Electrons are trapped on a helium surface by a pressing electric field. If the pressing electric field is perfectly perpendicular to the helium surface, the geometry has cylindrical symmetry with respect to the polar angle  $\theta$ , and no gradient is present ( $\lambda = 0$ ). However, a small misalignment angle  $\alpha$  between the electric field direction and the normal of the helium surface leads to an in-plane electric field component  $\alpha E_{\perp}$  ( $\alpha \ll 1$ ) which will create, within the local-density approximation, a density gradient  $\lambda = \chi \alpha E_{\perp}$ . Since we assume that the helium surface remains flat in the region where electrons are confined, the drift-diffusion equation (1) at the surface remains unchanged for finite  $\alpha$ , and it is only the relation between  $n_t$  and  $V_t$  which is changed when we use the exact nonlocal electrostatics. Since the normal of the electric field presents a discontinuity as it crosses the electrons on the helium cloud, a direct perturbation-theory expansion around the isotropic solution is not possible. We derived a suitable perturbation-theory expansion by performing a transformation into a curved set of coordinates where the position of the interface remains

fixed with  $\alpha$ . This expansion, to the lowest order, leads to a modified Laplace equation, which is given in the Appendix. Finite-element (FEM) [36] simulations based on this equation confirm the validity of the approximation  $n_{0c}(r) \simeq \alpha \chi E_{\perp} r$  for all the shapes of the electron cloud explored experimentally except near the edge of the electron cloud. Thus a small inclination of the helium surface with respect to the helium cell creates a well-defined density gradient which only weakly depends on the shape of the electron cloud  $n_0(r)$ . To simulate approximately the ac response of electrons on helium, we used the Poisson equation on the ac potential in the limit  $\alpha = 0$  and drift-diffusion equations on the helium surface to determine the expected admittance of the cell. The full equations and a discussion on their formal validity are provided in the Appendix.

We now present experiments that reveal the coexistence of one-dimensional (1D) EMPs and 2D GMPs; the simulations, which are presented simultaneously, will allow us to confirm the identification of the observed modes. The experiments were realized on an electron cloud (see Fig. 1) with  $N_e = 3 \times 10^7$  electrons at a magnetic field of  $B = 0.3$  T and temperature of 300 mK. The ac transport response of the electron cloud is measured in a Corbino geometry using a Sommer-Tanner method. An ac excitation voltage  $V_{ac}$  with a 30-mV amplitude is applied on the intermediate top-ring electrode at a frequency  $f_{ac}$  (1–10 kHz), and the induced pickup signal from the top central electrode is then measured with a voltage amplifier and a lock-in detector giving the ac cell admittance  $Y(f_{ac})$ . The position of magnetoplasmon resonances then shows as peaks in the admittance  $Y(f_{ac})$  for a fixed bias voltage  $V_b$ . This bias between the outer guard and central electrodes can tune the frequency of the magnetoplasmons by controlling the shape of the electron cloud [33,37]. For  $V_b < 0$  the electron cloud adopts a “plateau” density profile, where the density  $n_0(r)$  is a monotonously decaying function of the radial distance to the cloud center  $r$ , while for  $V_b > 0$  the electron density takes a “caldera” profile which has a density maximum inside the guard region at the edge of the electron cloud [Fig. 1(b)]. The EMPs which couple to the top measuring electrodes are different in the two regimes. For a plateau profile the outer edge of the cloud is closer to the center, and it is the EMPs propagating at the perimeter of the cloud which are detected. For a caldera geometry the cloud expands, and the outer perimeter becomes weakly coupled to the measurement electrodes; instead it is the interedge magnetoplasmons at the boundary between the guard and central regions which are more easily excited. To simplify further discussions, we will describe both situations as an EMP mode. The theoretical expressions for the propagation velocity are indeed similar in both cases [17,21]:

$$v_{\text{EMP}} \simeq \frac{\Delta n_e}{2\pi \epsilon_0 B} \ln \frac{1}{qh}, \quad (4)$$

where  $q$  is the wave vector ( $q = 1/R$  for the lowest-frequency mode, where  $R$  is the radius of the central bottom electrode) and  $\Delta n_e$  is the difference in electron density between the center and guard regions (this definition is discussed more precisely below).

For the magnetogradient plasmon the propagation velocity is given by

$$v_{\text{GMP}} \simeq \frac{\alpha E_{\perp}}{B\sqrt{2}}. \quad (5)$$

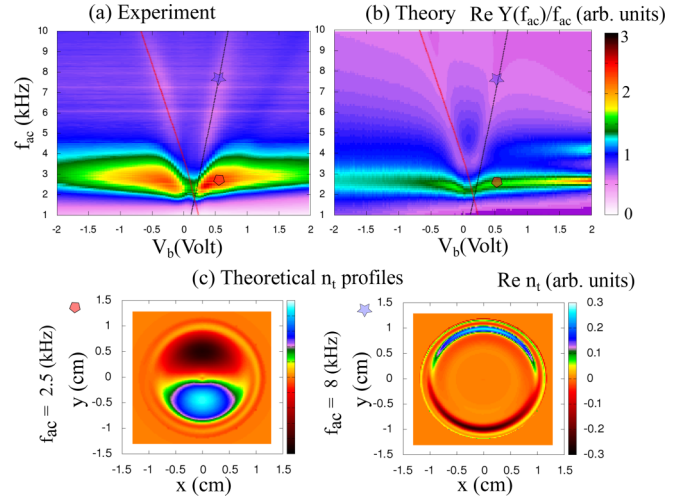


FIG. 2. (a) Magnetoplasmon modes appear as peaks in the real part of the cell admittance  $Y(f_{ac})$ , which is shown here as a function of the density profile (controlled by the bias  $V_b$  between guard and central regions) and excitation frequency  $f_{ac}$ . Two magnetoplasmon modes are observed in the explored frequency range with very different dependence on  $V_b$ : a dispersing mode at higher frequency (branch carrying the star symbol) and a low-frequency mode (branch carrying the pentagon symbol) with very small dependence of the electron cloud density profile. (b) Finite-element simulations of  $Y(f_{ac})$  based on Eq. (1) taking into account a small tilt  $\alpha = 0.4^\circ$  (fitted to data). (c) Theoretical oscillating density profiles ( $n_t$ ); the low-frequency “magnetogradient” plasmon ( $n_t$  at the pentagon symbol) is delocalized across the entire electron cloud, whereas the higher-frequency plasmon ( $n_t$  at the star symbol) is an edge magnetoplasmon (or interedge at  $V_b > 0$ ) propagating in one dimension. The two modes seem to make an avoided crossing when their frequencies overlap near  $V_b = 0$ .

This expression is obtained from Eq. (3) using the approximation  $\lambda = \alpha \chi E_{\perp}$ . It depends on the perpendicular electric field  $E_{\perp}$  but not on  $\Delta n_e$  as opposed to the EMP modes. This difference in the  $\Delta n_e$  dependence provides a convenient method to distinguish between GMP and EMP modes. We represent the admittance  $Y(f_{ac})$  as a function of both  $V_b$  and  $f_{ac}$  as a color-scale map that allows us to visualize the dependence of the mode frequency on the voltage  $V_b$  (and thus on  $\Delta n_e$ ). Modes that “disperse” as a function of  $V_b$  are candidate 1D EMP modes, while the absence of a  $V_b$  dependence suggests a magnetogradient mode.

Our experimental results are shown in Fig. 2 together with FEM simulations of the perturbation theory that we introduced. Both experiment and simulations show the presence of two resonant modes at low frequency: a mode whose frequency strongly depends on  $V_b$  with a dependence that reminds us of the dispersion relation of “Dirac” fermions and a second mode whose frequency is almost independent of  $V_b$  except when its frequency crosses the frequency of the dispersive mode.

To identify the dispersive mode as an EMP, we show the theoretical frequency expected from Eq. (4). For the caldera geometry [positive  $V_b$ , black lines in Figs. 2(a) and 2(b)], we set  $\Delta n_e$  as the difference between the electron density on top of the rim in the guard region and the density in the center

of the electron cloud; it reproduces the experimental EMP frequency without adjustable parameters. The EMP modes should not be visible in Corbino geometry, and the FEM simulations show that a small tilt of the helium cell can explain their contribution to the Corbino signal with an amplitude comparable to that of the experiment. For the plateau geometry (red lines for negative  $V_b$ ) the density in the guard entering in  $\Delta n_e$  had to be reduced by 20% compared with its maximum density in the guard. This phenomenological correction probably reflects a more complex situation where the electron cloud boundary moves with  $V_b$  as the cloud is pushed towards the center. FEM simulations predict the correct position for the EMP mode without adjustable parameters even in this case. The predictions for the linewidth and admittance amplitude are less accurate as they are dependent on the ratio  $\mu_{xx}/\mu_{xy}$ , which was assumed to be fixed to  $5 \times 10^{-3}$  and without any density dependence. To confirm the 1D character of this dispersive mode, we also represented the simulated oscillating density profile  $n_t$  of the EMP mode in Fig. 2: The oscillating density is indeed localized in a narrow strip of width  $h$  at the boundary between the central and guard regions. Note that the perturbation theory is not reliable at the outer edge of the electron cloud and the peak in  $n_t$  on the outer cloud boundary may not be physical.

The lowest-frequency mode in Fig. 2 has a resonance frequency which is independent of  $V_b$  except near the crossing points with the previously identified EMP mode. It is thus a candidate GMP mode. To confirm this assignment, we checked that this frequency scales as  $\propto E_{\perp}/B$  as expected from Eq. (5). The only other parameter in Eq. (5) is the inclination of the helium free surface  $\alpha$  compared with the electric field. It was not possible to control this angle precisely in our experiment; however, we confirmed that this frequency changes indeed with a small variation (of around  $0.1^\circ$ ) of the refrigerator inclination. These experiments are shown in the Appendix (see Fig. 8). The FEM simulations allow us to visualize the oscillating density profile, which is displayed in Fig. 2; this mode is delocalized across the entire electron cloud. In the Appendix, in Fig. 6, we present experiments with segmented pickup electrodes which allow us to confirm some features of the GMP density distribution. A good agreement between simulations and the experimental Girvin-MacDonald-Platzman (GMP) mode is obtained for  $\alpha = 0.4^\circ$ . At the crossing between GMP and EMP at  $V_b = 0$  both simulations and experiment suggest an avoided crossing, which implies the exciting possibility of realizing hybrid states with simultaneous characteristics of a one-dimensional topological EMP and a delocalized two-dimensional mode [note that changes in the GMP confinement potential also contribute to the change in the GMP frequency at  $V_b = 0$ ; this contribution is discussed in the Appendix (see Fig. 3)]. Concerning the linewidth of GMP modes, the simulations predict a similar linewidth to that of the edge-magnetoplasmon modes. This contrasts with the experiment where the GMP is significantly broader than the EMP with a linewidth that depends on  $V_g$ . This could be due to the dependence of the mobility on the electron density, which is not taken into account in the model. Indeed, the GMP is delocalized and thus can be more sensitive to mobility gradients which appear as a result of the density variations across the electron cloud. In the data in Fig. 2 the

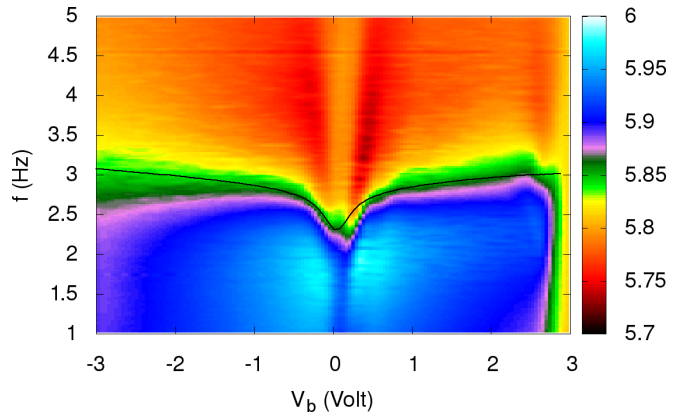


FIG. 3. Imaginary part of the cell admittance  $\text{Im} Y / f_{\text{ac}}$  (in arbitrary units) for the experimental parameters of Fig. 2; the admittance of the cell mainly behaves as a capacitance and is thus divided by  $f_{\text{ac}}$  to compensate its linear increase with frequency. The position of the GMP resonance is given by the green contour curves, and the lowest eigenfrequency of the effective Schrödinger equation for  $\alpha = 0.4^\circ$  is shown by the black line.

quality factor of the GMP resonance is not so high; however, in the Appendix we show experimentally that the quality factor increases substantially with stronger perpendicular field (as shown in Fig. 7), with tilt angle (Fig. 8), or at minima of microwave-induced resistance oscillations (Fig. 9), proving that GMP is a genuine resonance of the 2D electron system.

#### IV. CONCLUSION

To summarize, we have shown both theoretically and experimentally that a system of electrons on the surface of liquid helium hosts a novel type of bulk excitation, the delocalized two-dimensional magnetogradient plasmon modes which appear in the presence of a small density gradient. This system provides a highly controllable environment in which the interaction of this novel excitation with the previously known (topological) one-dimensional edge magnetoplasmons may be studied. As gradients of carrier concentration can easily be present in mesoscopic devices, this mode can also be present in new two-dimensional electron systems.

#### ACKNOWLEDGMENTS

We acknowledge fruitful discussions with D. L. Shepelyansky and M. Dykman and thank ANR SPINEX for financial support.

#### APPENDIX

##### 1. DERIVATION OF THE MAIN EQUATIONS

###### a. Derivation of the effective Schrödinger equation

The following equation is derived from the drift-diffusion equations written in the local-density approximation:

$$\partial_t \begin{Bmatrix} n_{t0} \\ n_{tc} \\ n_{ts} \end{Bmatrix} = \frac{\mu_{xy}}{\chi r} \begin{Bmatrix} \lambda \partial_r (r n_{ts}) / 2 \\ n_{ts} \partial_r n_0 \\ \lambda r \partial_r n_{t0} - n_{tc} \partial_r n_0 \end{Bmatrix} \quad (\text{A1})$$

The density gradient  $\lambda$  introduces a coupling between different angular harmonics of the electron density. Introducing the effective wave function  $\psi(r) = \sqrt{r}n_{ls}$ , this equation can be reduced to the effective Schrödinger equation

$$\frac{\chi^2 \omega^2}{\mu_{xy}^2} \psi = -\frac{\lambda^2}{2} \partial_r^2 \psi + \frac{3\lambda^2}{8r^2} \psi + \frac{(\partial_r n_0)^2}{r^2} \psi, \quad (\text{A2})$$

where  $\lambda = \frac{4\epsilon_0 \alpha E_{\perp}}{he}$ , which is Eq. (3) from the main text. We remind the reader that the only unknown parameter in this theory is the cell tilt angle  $\alpha$ ; we set it to  $\alpha = 0.4^\circ$  as in the finite-element simulations.

Figure 3 shows a comparison between the experimental position of the GMP resonance and the predictions of the effective Schrödinger equation for the data from Fig. 2. The position of the resonance is more easily followed on the out-of-phase response, as it corresponds to a constant value contour. The color in Fig. 3 thus shows  $\text{Im} Y$  (instead of  $\text{Re} Y$  as in Fig. 2) as a function of the bias voltage  $V_b$  and the excitation. The position of the resonance corresponds to the green contour curves. We see that Eq. (3) gives a satisfactory description of the dependence of the resonance frequency as a function of  $V_b$ . However, the effective theory does not capture the double resonance structure near  $V_b = 0$  since it appears due to the crossing between the GMP and EMP modes, which is not taken into account in this simplified model.

#### b. Effective Poisson equation in deformed coordinates where the position of the helium layer is fixed

To enable the use of standard perturbation series, we thus need to perform a coordinate transformation which levels the helium surface in the cell while keeping in place the top and bottom electrodes. We choose a rotation in the  $(x, z)$  plane (containing the electric field direction  $z$  and the slightly misaligned helium surface normal) with a height-dependent rotation angle  $\phi(z) = \alpha(1 - \frac{z^2}{h^2})$ . The transformation between coordinates is then realized by

$$\begin{pmatrix} x \\ z \end{pmatrix} = \begin{pmatrix} \cos \phi(z')x' - \sin \phi(z')z' \\ \sin \phi(z')x' + \cos \phi(z')z' \end{pmatrix}, \quad (\text{A3})$$

where  $x', z'$  are the new coordinates.

In the new coordinates the Poisson equation, to first order in  $\alpha$ , becomes

$$\Delta V + \frac{8\alpha}{h^2} (x\partial_z V + 2xz\partial_z^2 V - 3z\partial_x V - 2z^2\partial_{xz} V) = 0; \quad (\text{A4})$$

in this form it can be expanded in powers of  $\alpha$ . We see from Eq. (A4) that  $\alpha$  induces a coupling only between neighboring angular harmonics; thus, to first order in  $\alpha$ , to which we will limit ourselves here, only  $\cos \theta$  and  $\sin \theta$  terms will be generated.

We solved Eq. (A4) for a stationary electron cloud without ac excitation; this allows us to find the static density profile  $n_a(r, \theta) = n_0(r) + \alpha n_{0c}(r) \cos \theta$  induced by the tilt of the cell. In the stationary case the potential of the electron cloud is constant and fixed by the total charge of the cloud. In the isotropic case the problem then reduces to find a stable boundary of the electron cloud for which the electric field at the boundary vanishes, which was done in a systematic way for different geometries in Ref. [33]. To find the anisotropic correction

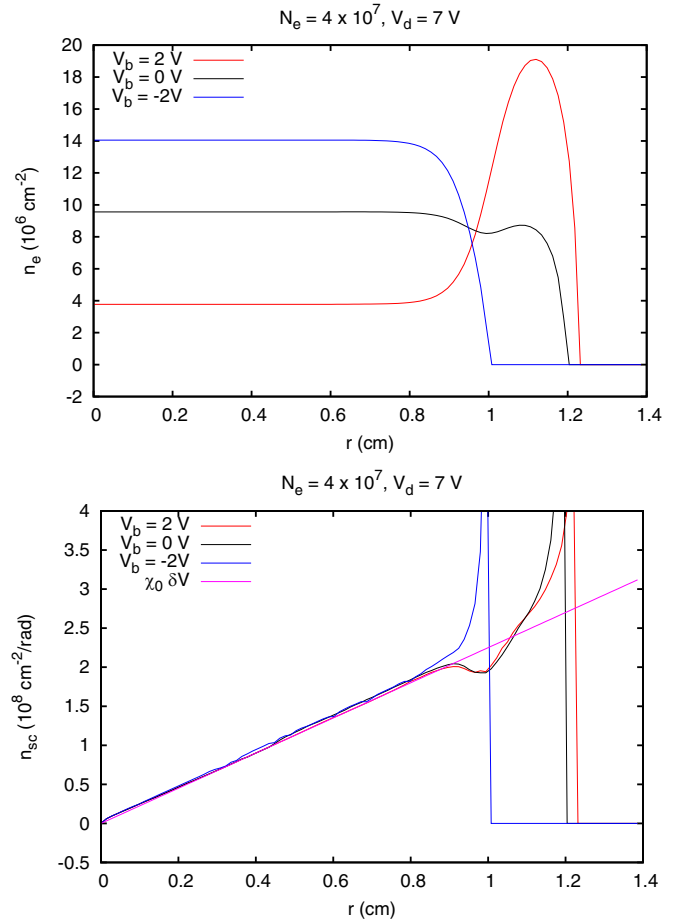


FIG. 4. The top panel shows the evolution of the radial steady-state density  $n_0(r)$  for different bias voltages  $V_b$  between central and guard reservoirs. The bottom panel shows the tilted component of density  $n_{0c}$  under the same conditions [we remind the reader that the total steady-state density is the sum  $n_0(r) + \alpha n_{0c}(r) \cos \theta$ ];  $n_{0c}$  depends only weakly on  $V_b$  in contrast to  $n_0(r)$  and is well approximated by  $n_{0c} = \chi \alpha E_{\perp} r$  (straight line).

$n_{0c}(r)$ , we iterated Eq. (A4) neglecting the small deformation of the circular cloud boundary. While this approach should give accurate predictions in the center of the electron cloud, the validity of the perturbation theory breaks down near the cloud boundary. The results of our finite-element calculations for  $n_0(r)$  and  $n_{0c}(r)$  are shown in Fig. 4.

To be fully consistent, we in principle need to use the modified Poisson Eq. (A4), which introduces a mixing between harmonics due to the tilt; we found, however, that using the usual Poisson equation  $\Delta V = 0$  already gives a good description of the experiment. This probably comes from the fact that the dynamic drift-diffusion equations already introduce a coupling between modes through the density gradient  $n_{0c}$  and many (but seemingly not all) of the terms that would come from Eq. (A4) become second order in  $\alpha$ .

#### c. Full drift-diffusion equations for the lowest angular harmonics

For reference we write the full drift-diffusion equations as a function of the steady-state radial distribution  $n_0$  and the density gradient  $n_{0c}$  including contributions from both  $\mu_{xx}$  and  $\mu_{xy}$ ; these are the equations which are solved to build Fig. 2.

The ac potential  $V_t$  is decomposed into its lowest harmonics  $V_t = V_{t0}(r) + V_{tc}(r) \cos \theta + V_{ts}(r) \sin \theta$ .

$$\partial_t \begin{Bmatrix} n_{t0} \\ n_{tc} \\ n_{ts} \end{Bmatrix} = \frac{\mu_{xy}}{r} \begin{Bmatrix} \frac{1}{2} \partial_r (n_{sc} V_{ts}) \\ V_{ts} \partial_r n_0 \\ n_{sc} \partial_r V_{t0} - V_{tc} \partial_r n_0 \end{Bmatrix} + \frac{\mu_{xx}}{r} \begin{Bmatrix} \partial_r [r(n_0 \partial_r V_{t0} + \frac{1}{2} n_{sc} \partial_r V_{tc})] \\ \partial_r [r(n_0 \partial_r V_{tc} + n_{sc} \partial_r V_{t0})] - \frac{n_0}{r} V_{tc} \\ \partial_r [r(n_0 \partial_r V_{ts})] - \frac{n_0}{r} V_{ts} \end{Bmatrix}. \quad (\text{A5})$$

## 2. Probing the spatial structure of the GMP

The system of equations (A1) gives a relation between the time derivative of the polar angle average of the electron density  $\partial_t n_{t0}$  and the radial derivatives of its first angular harmonic  $n_{ts}$ :

$$\partial_t n_{t0} = \frac{\lambda \mu_{xy}}{2 \chi r} \partial_r (r n_{ts}). \quad (\text{A6})$$

This relation gives insight into the spatial structure of the GMP mode, which is most easily visualized by plotting both the in-phase and out-of-phase density maps, which are both displayed in Fig. 5; note that Fig. 2 for compactness only showed  $\text{Re } n_t$ . We see that while the in-phase density response is dominated by the  $\sin \theta$  angular harmonic, the out-of-phase component is essentially isotropic.

This observation can be checked in experiments with segmented Corbino electrodes, which can probe not only the polar-angle-averaged electron density but also its angular harmonics. We performed such experiments using the electrode layout shown in Fig. 6, where in contrast to the experiments in the Corbino geometry, the excitation was applied on the top central electrode. The detection was performed on the surrounding ring electrode which was split into four segments (named after the cardinal directions). Four voltage amplifiers were connected to each of the segments, to measure the admittance  $Y_s$  between the central electrodes and the segments. As previously  $Y$  is shown rescaled by  $f_{ac}$  due to the mainly capacitive behavior of the admittance.

The results of the experiments are shown in Fig. 6 together with finite-element simulations of the expected voltage on the segmented electrodes (obtained by angular integration of  $n_{t0}$ ,  $n_{tc}$ , and  $n_{ts}$ ). We see that the spatial structure of the mode GMP gives rise to a rather counterintuitive behavior: The signal measured on individual segments seems out of phase

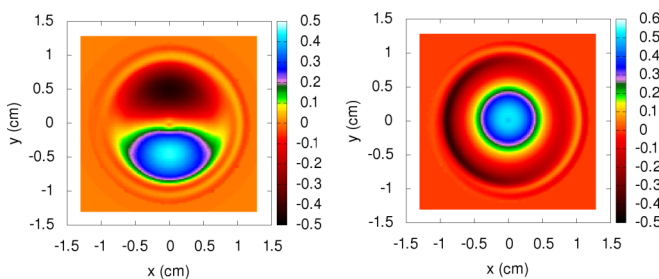


FIG. 5. Time-dependent part of the electron density as a function of the spatial coordinates  $x$  and  $y$ , calculated for the following parameters: saturation voltage  $V_{\text{sat}} = 0.8$  V,  $V_b = 0$  V,  $V_d = 7.5$  V,  $B = 0.23$  T, and  $f_{ac} = 2.5$  kHz (pentagon symbol in Fig. 2). The electron density has both an in-phase component  $\text{Re } n_t$  (left panel) and an out-of-phase component  $\text{Im } n_t$  (right panel) with respect to the excitation voltage.

with respect to the sum signal from all the segments. For example, the imaginary part of the admittance from the segments is mainly an in-phase resonance line shape, with a peak at resonance; however, the sum from all the segments behaves more like a derivative feature (dispersive out-of-phase signal).

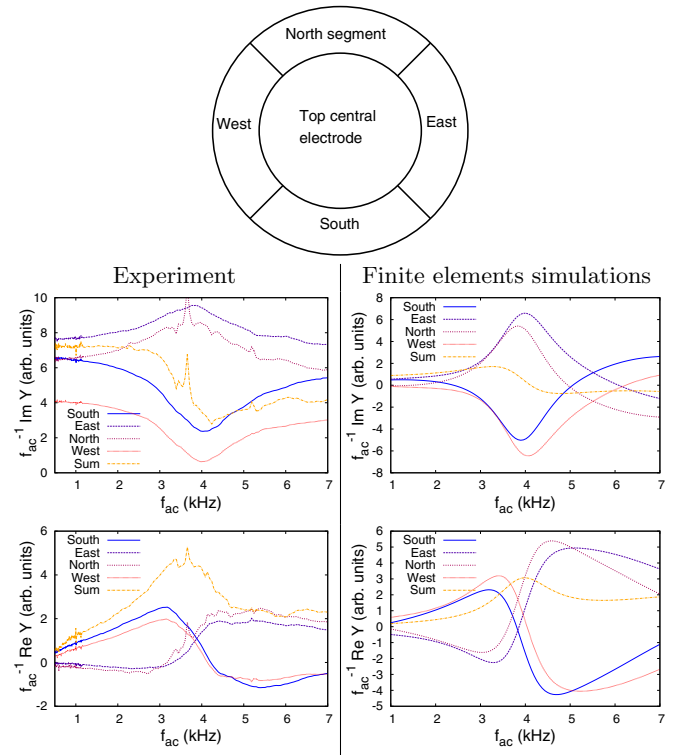


FIG. 6. Admittance measurements from segmented electrodes; gate voltages were set to  $V_b = 0$  V and  $V_d = 7.5$  V, the perpendicular magnetic field was  $B = 0.23$  T, the total electron number was  $N_e = 2 \times 10^7$ , and the temperature was 0.2 K. In the finite-element simulations we used the numerical values  $\alpha = 0.5^\circ$  and  $\mu_{xx}/\mu_{xy} = 2 \times 10^{-2}$ . The signal from individual segments and the isotropic signal (sum of all segments) are dephased by  $90^\circ$  with each other, displaying different line shapes: peaked and dispersive for the real and imaginary parts of the admittance, respectively. This unusual behavior is reproduced by the finite-element simulations and illustrates the spatial structure of the oscillating electron density shown in Fig. 5. The signal is shown in arbitrary units since when measurements are done with a voltage amplifier the measured voltage depends on the capacitance of the measuring cables and a careful calibration is needed to recover the absolute value of the admittance. We showed in Ref. [33] that with such calibrations the contribution of the electron gas to the measured capacitance perfectly agrees with the finite-element simulations (except for zero-resistance states). We thus feel justified here not to focus on the relative scales between the experimental and theoretical signals as we know that their amplitudes coincide in the limit of low frequencies and use arbitrary units for simplicity.

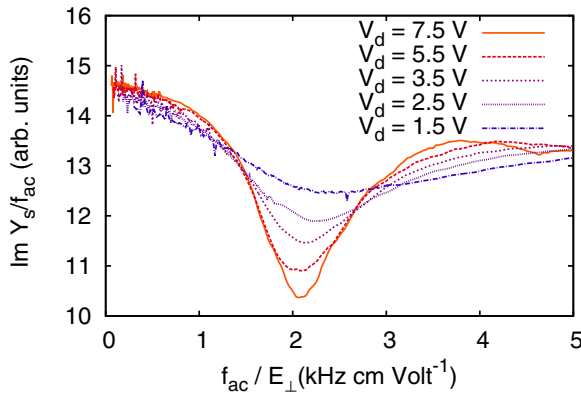


FIG. 7. The frequency of the GMP mode is proportional to the perpendicular electric field as predicted. The imaginary part of the admittance of one of the segments (see discussion on the phase of the resonance in Sec. 2 of the Appendix) is shown as a function of the excitation frequency  $f_{ac}$ , the bias voltage is set to zero ( $V_b = 0$ ), and the perpendicular electric field is given by  $E_{\perp} = V_d/h$  ( $h = 2.6$  mm),  $B = 0.23$  T. The excitation frequency  $f_{ac}$  is divided by the perpendicular electric field, so that the position of the resonance remains fixed when  $E_{\perp}$  is changed (different curves correspond to different  $E_{\perp}$ ). The quality factor of the resonance increases with increasing  $E_{\perp}$ .

Similarly, the real part of the admittance from individual segments behaves as a derivative (dispersive line shape), while the sum from all segments follows the line shape of an in-phase resonance. This  $90^\circ$  phase shift between the admittance of a single segment and the isotropic average overall signal is nicely reproduced in the finite-element simulations and is a manifestation of the spatial structure of the oscillating charge density shown in Fig. 5, where the  $\sin \theta$  angular harmonic and the isotropic component are out of phase with each other.

### 3. Perpendicular electric field dependence

Figure 7 shows that the frequency of the GMP mode is proportional to the perpendicular electric field as predicted.

### 4. Tilting the refrigerator

In the experiment shown in Fig. 8, we check that the frequency of the GMP mode can be changed by tilting the refrigerator, which modifies the angle  $\alpha$ ; the change in the resonance frequency is shown in the top panel with an increase in the resonance quality factor. The increase in the tilt angle was estimated from the shift of the GMP mode. It was not possible to confirm this value independently since the design of our refrigerator was not optimized to allow the fine-tuning of its inclination with respect to the vertical direction (the estimated change is consistent with the indications of the bubble level meters that were fixed on the refrigerator). We are, however, certain that all other parameters remained fixed while the refrigerator was tilted. The gate voltages were fixed [ $V_b = 2$  V (in the top panel),  $V_d = 7$  V], and the trapped magnetic field remained  $B = 0.3$  T. The only parameter that could change is in fact the number of electrons trapped in the cloud as electrons could escape during the mechanical motion of the refrigerator. We confirmed that this was not the case in the bottom panel, which shows scans of the cell admittance

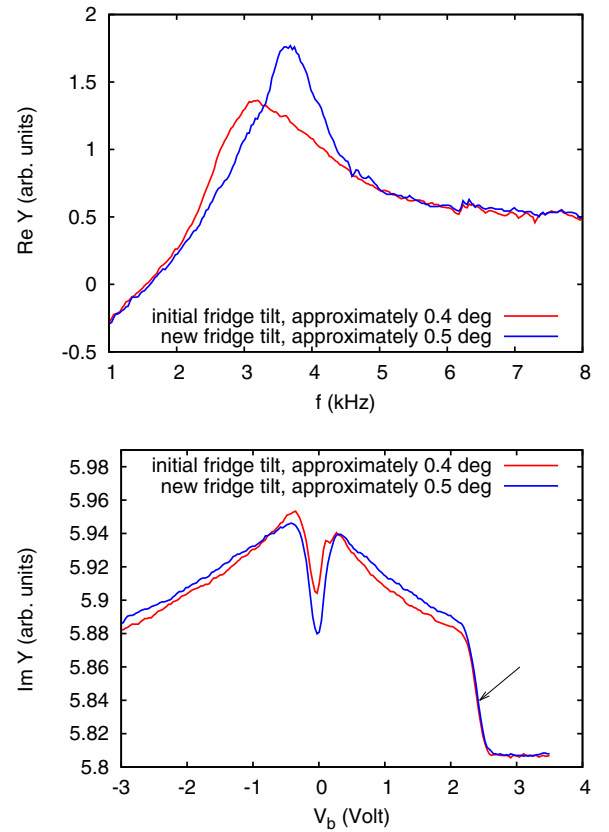


FIG. 8. The top panel shows that the frequency of the GMP mode can be changed by tilting the refrigerator, which modifies the angle  $\alpha$ ; the change in the resonance frequency is shown in the top panel with an increase in the resonance quality factor. The bottom panel confirms that the number of trapped electrons did not change as the refrigerator was tilted.

as a function of the bias voltage  $V_b$  before and after the tilt at  $f_{ac} = 1.137$  kHz. The voltage threshold indicated by the black arrow at which the central region of the cell becomes filled with electrons is directly related to the total number of trapped electrons; it did not change before and after the tilt allowing us to confirm that  $N_e = 3 \times 10^7$  did not change during the tilt of the refrigerator.

### 5. Gradient magnetoplasmons under microwave irradiation

We have shown that increasing the perpendicular electric field  $E_{\perp}$  and the tilt angle  $\alpha$  increases the quality factor of the GMP resonance; this probably occurs because the resonance frequency increases while the loss rate remains fixed. It is also possible to reduce the damping by applying microwave irradiation at a frequency which can induce zero-resistance states. The modulation of the GMP resonance in this case is shown in Fig. 9 for two values of  $N_e$ . When a microwave frequency at resonance between the lowest and first excited Rydberg state is sent into the cell (at the intersubband resonance in quantum well terminology), a  $1/B$  periodic modulation of the quality factor of the GMP resonance is observed. At conditions corresponding to minima of the microwave-induced resistance oscillations the quality factor of the GMP resonance is substantially increased. Figure 9 also shows the admittance

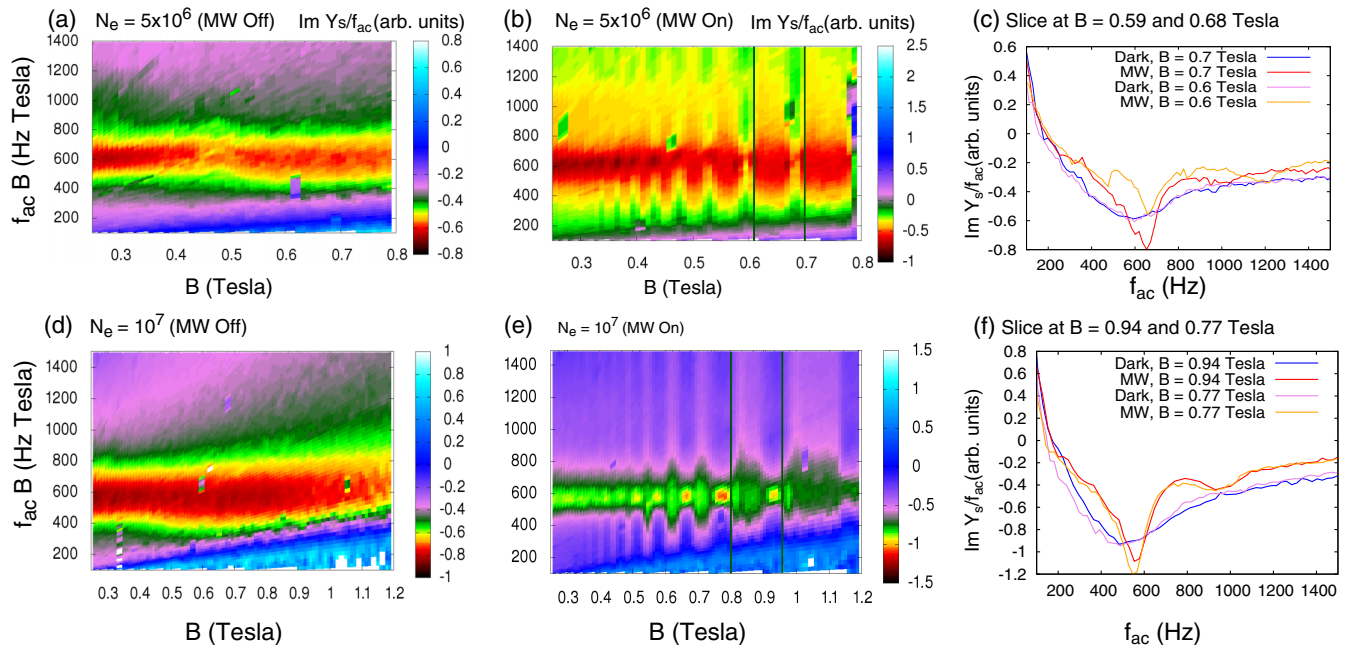


FIG. 9. The color-scale diagrams [(a), (b), (d), and (e)] show the imaginary part of the admittance from one segment (see Fig. 6 for a discussion on the phase of the signal) measured as a function of the perpendicular magnetic field  $B$  and the low-frequency ac excitation frequency  $f_{ac}$ . In the figure this frequency is multiplied by  $B$  to emphasize the  $1/B$  dependence of the GMP resonance; indeed, with this rescaling the position of the resonance remains fixed as the magnetic field is varied. Experiments are shown both in the dark and under microwave (MW) irradiation at 139 GHz, a frequency which excites the transition between the two lowest-lying Rydberg levels leading to microwave-induced resistance oscillations which appear in (b) and (e) as a  $1/B$  periodic modulation of the GMP resonance quality factor. As shown in the data slices in (c) and (f) the quality factor of the GMP resonance substantially increases at minima of the microwave-induced resistance oscillations. (a)–(c) correspond to  $N_e = 5 \times 10^6$ , while (d)–(f) were obtained for  $N_e = 10 \times 10^6$ . In both cases the gate voltages were  $V_d = 4.5$  V and  $V_b = -3.5$  V.

$Y(f_{ac})$  without microwaves confirming that the frequency of the GMP resonance scales as  $1/B$  as a function of  $B$ ; interestingly, without microwave irradiation the quality factor of the resonance does not seem to depend much on the magnetic field. This is probably due to an approximate compensation between the  $1/B$  decrease in the resonance frequency and the  $1/B$  decrease in the ratio  $\mu_{xx}/\mu_{xy}$ . Experimentally, this leads to a plateau where the admittance of the cell becomes independent of the magnetic field; thus due to the contribution of the GMP mode an admittance plateau can appear even when  $\mu_{xx}$  still decreases with the magnetic field.

While we do not yet have a model for the resonant modes in the zero-resistance state, it seems very likely that excitation of the GMP mode plays an important role in the transition to the zero-resistance state (ZRS). Experimentally, self-oscillations at frequencies consistent with the GMP mode were reported in Ref. [35]. We also showed that the ZRS for electrons on helium is a collective state where the microwave excitation must be at resonance with the transition between the lowest Rydberg levels in the entire system (intersubband resonance); detuning the edge of the electron cloud is enough to suppress the ZRS in the center of the cloud even if the edge is

separated from the center by a macroscopic distance larger than the electrostatic screening length [33]. GMP is a collective mode spreading through the entire electron cloud and seems well placed to explain this collective behavior. Note that in these experiments, anomalous compressibility values (negative) were found close to  $V_b = 0$ , a value that we now understand to be singular for the resonance frequency of GMP. Finally, we also know that due to inhomogeneous broadening, only a small fraction of the electrons in the system should actually be at resonance with the microwave photons; yet the collective response seems to suggest that all the electrons are excited. The GMP mode can also provide an explanation for these apparently conflicting observations. Indeed, the density oscillations in the GMP mode will also create an oscillation of the perpendicular electric field. If the amplitude of the GMP oscillation is sufficiently large, it can locally compensate the detuning due to the static inhomogeneous broadening. In this case, during a cycle of the GMP mode all the electrons will cross the resonance and will be excited at least once in a GMP oscillation period. These arguments show that accurate modeling of the GMP resonance is an important step in the understanding of zero-resistance states for electrons on helium.

- [1] C. L. Kane and E. J. Mele, *Phys. Rev. Lett.* **95**, 226801 (2005).  
 [2] B. Bernevig, T. Hughes, and S. Zhang, *Science* **314**, 1757 (2006).

- [3] M. König, S. Wiedmann, C. Brüne, A. Roth, H. Buhmann, L. W. Molenkamp, X.-L. Qi, and S.-C. Zhang, *Science* **318**, 766 (2007).  
 [4] L. Fu and C. L. Kane, *Phys. Rev. B* **76**, 045302 (2007).

- [5] S. Murakami, *New J. Phys.* **9**, 356 (2007).
- [6] D. Hsieh, D. Qian, L. Wray, Y. Xia, Y. S. Hor, R. J. Cava, and M. Z. Hasan, *Nature (London)* **452**, 970 (2008).
- [7] Y. L. Chen, J. G. Analytis, J.-H. Chu, Z. K. Liu, S.-K. Mo, X. L. Qi, H. J. Zhang, D. H. Lu, X. Dai, Z. Fang, S. C. Zhang, I. R. Fisher, Z. Hussain, and Z.-X. Shen, *Science* **325**, 178 (2009).
- [8] A. A. Taskin, Z. Ren, S. Sasaki, K. Segawa, and Y. Ando, *Phys. Rev. Lett.* **107**, 016801 (2011).
- [9] I. Knez, R.-R. Du, and G. Sullivan, *Phys. Rev. Lett.* **107**, 136603 (2011).
- [10] A. Murani, A. Kasumov, S. Sengupta, Y. A. Kasumov, V. T. Volkov, I. I. Khodos, F. Brisset, R. Delagrèange, A. Chepelianskii, R. Deblock, H. Bouchiat, and S. Guéron, *Nat. Commun.* **8**, 15941 (2017).
- [11] F. Schindler, Z. Wang, M. G. Vergniory, A. M. Cook, A. Murani, S. Sengupta, A. Y. Kasumov, R. Deblock, S. Jeon, I. Drozdov, H. Bouchiat, S. Guéron, A. Yazdani, B. A. Bernevig, and T. Neupert, *Nat. Phys.* **14**, 918 (2018).
- [12] E. B. Olshanetsky, Z. D. Kvon, G. M. Gusev, A. D. Levin, O. E. Raichev, N. N. Mikhailov, and S. A. Dvoretzky, *Phys. Rev. Lett.* **114**, 126802 (2015).
- [13] S. Mueller, A. N. Pal, M. Karalic, T. Tschirky, C. Charpentier, W. Wegscheider, K. Ensslin, and T. Ihn, *Phys. Rev. B* **92**, 081303(R) (2015).
- [14] D. C. Glattli, E. Y. Andrei, G. Deville, J. Poitrenaud, and F. I. B. Williams, *Phys. Rev. Lett.* **54**, 1710 (1985).
- [15] D. B. Mast, A. J. Dahm, and A. L. Fetter, *Phys. Rev. Lett.* **54**, 1706 (1985).
- [16] I. Petković, F. I. B. Williams, K. Bennaceur, F. Portier, P. Roche, and D. C. Glattli, *Phys. Rev. Lett.* **110**, 016801 (2013).
- [17] V. A. Volkov and S. A. Mikhailov, *Zh. Eksp. Teor. Fiz.* **94**, 217 (1988) [*Sov. Phys. JETP* **67**, 1639 (1988)].
- [18] D. Jin, L. Lu, Z. Wang, C. Fang, J. D. Joannopoulos, M. Soljacic, L. Fu, and N. X. Fang, *Nat. Commun.* **7**, 13486 (2016).
- [19] D. Jin, Y. Xia, T. Christensen, M. Freeman, S. Wang, K. Y. Fong, G. C. Gardner, S. Fallahi, Q. Hu, Y. Wang, L. Engel, Z.-L. Xiao, M. J. Manfra, N. X. Fang, and X. Zhang, *Nat. Commun.* **10**, 4565 (2019).
- [20] T. Ozawa, H. M. Price, A. Amo, N. Goldman, M. Hafezi, L. Lu, M. C. Rechtsman, D. Schuster, J. Simon, O. Zilberberg, and I. Carusotto, *Rev. Mod. Phys.* **91**, 015006 (2019).
- [21] V. A. Volkov and S. A. Mikhailov, *Landau Level Spectroscopy*, Modern Problems in Condensed Matter Sciences Vol. 27 (1991), Chap. 15, p. 855.
- [22] P. L. Elliott, C. I. Pakes, L. Skrbek, and W. F. Vinen, *Phys. Rev. Lett.* **75**, 3713 (1995).
- [23] I. L. Aleiner, D. Yue, and L. I. Glazman, *Phys. Rev. B* **51**, 13467 (1995).
- [24] M. A. Zudov, R. R. Du, J. A. Simmons, and J. L. Reno, *Phys. Rev. B* **64**, 201311(R) (2001).
- [25] P. Ye and L. Engel, *Appl. Phys. Lett.* **79**, 2193 (2001).
- [26] R. Mani, J. H. Smet, K. von Klitzing, V. Narayanamurti, W. B. Johnson, and V. Umansky, *Nature (London)* **420**, 646 (2002).
- [27] M. A. Zudov, R. R. Du, L. N. Pfeiffer, and K. W. West, *Phys. Rev. Lett.* **90**, 046807 (2003).
- [28] R. G. Mani, A. N. Ramanayaka, and W. Wegscheider, *Phys. Rev. B* **84**, 085308 (2011).
- [29] Y. P. Monarkhaa, *Low Temp. Phys.* **37**, 655 (2011).
- [30] I. A. Dmitriev, A. D. Mirlin, D. G. Polyakov, and M. A. Zudov, *Rev. Mod. Phys.* **84**, 1709 (2012).
- [31] D. Konstantinov and K. Kono, *Phys. Rev. Lett.* **103**, 266808 (2009).
- [32] D. Konstantinov and K. Kono, *Phys. Rev. Lett.* **105**, 226801 (2010).
- [33] A. D. Chepelianskii, M. Watanabe, K. Nasyedkin, K. Kono, and D. Konstantinov, *Nat. Commun.* **6**, 7210 (2015).
- [34] D. Konstantinov, A. Chepelianskii, and K. Kono, *J. Phys. Soc. Jpn.* **81**, 093601 (2012).
- [35] D. Konstantinov, M. Watanabe, and K. Kono, *J. Phys. Soc. Jpn.* **82**, 075002 (2013).
- [36] F. Hecht, *J. Numer. Math.* **20**, 251 (2012).
- [37] A. Chepelianskii, M. Watanabe, and K. Kono, *J. Low Temp. Phys.* **195**, 307 (2019).